HHS Public Access

Author manuscript

IEEE Trans Med Imaging. Author manuscript; available in PMC 2023 July 01.

Published in final edited form as:

IEEE Trans Med Imaging. 2022 July ; 41(7): 1802–1812. doi:10.1109/TMI.2022.3149421.

Modeling Bias Error in 4D flow MRI Velocity Measurements

Sean M. Rothenberger,
Weldon School of Biomedical Engineering, Purdue University, West Lafayette, IN 47907 USA

Jiacheng Zhang,
School of Mechanical Engineering, Purdue University, West Lafayette, IN 47907 USA

Melissa C. Brindise,
School of Mechanical Engineering, Purdue University, West Lafayette, IN 47907 USA

Susanne Schnell,
Institute for Physics, Universität Greifswald, Germany

Michael Markl,
Department of Radiology at the Feinberg School of Medicine, Northwestern University, Chicago, IL 60611 USA

Pavlos P. Vlachos,
Weldon School of Biomedical Engineering and School of Mechanical Engineering, Purdue University, West Lafayette, IN 47907 USA

Vitaliy L. Rayz
Weldon School of Biomedical Engineering and School of Mechanical Engineering, Purdue University, West Lafayette, IN 47907 USA

Abstract

We present a model to estimate the bias error of 4D flow magnetic resonance imaging (MRI) velocity measurements. The local instantaneous bias error is defined as the difference between the expectation of the voxel's measured velocity and actual velocity at the voxel center. The model accounts for bias error introduced by the intra-voxel velocity distribution and partial volume (PV) effects. We assess the intra-voxel velocity distribution using a 3D Taylor Series expansion. PV effects and numerical errors are considered using a Richardson extrapolation. The model is applied to synthetic Womersley flow and *in vitro* and *in vivo* 4D flow MRI measurements in a cerebral aneurysm. The bias error model is valid for measurements with at least 3.75 voxels across the vessel diameter and signal-to-noise ratio greater than 5. All test cases exceeded this diameter to voxel size ratio with diameters, isotropic voxel sizes, and velocity ranging from 3–15mm, 0.5–1mm, and 0–60cm/s, respectively. The model accurately estimates the bias error in voxels not affected by PV effects. In PV voxels, the bias error is an order of magnitude higher, and the accuracy of the bias error estimation in PV voxels ranges from 67.3% to 108% relative to the actual bias error. The bias error estimated for *in vivo* measurements increased two-fold at systole compared to diastole in partial volume and non-partial volume voxels, suggesting the bias

vlrayz@purdue.edu .

error varies over the cardiac cycle. This bias error model quantifies 4D flow MRI measurement accuracy and can help plan 4D flow MRI scans.

Keywords

Hemodynamics; Magnetic Resonance Velocimetry (MRV); partial volume effects; Phase Contrast Magnetic Resonance Imaging (PC-MRI); systematic error

I. INTRODUCTION

4D flow magnetic resonance imaging (MRI) is a phase contrast-MRI (PC-MRI) technique that provides time-resolved velocity measurements in three directions and has medical utility for quantifying cardiovascular flows *in vivo*. 4D flow MRI accuracy is of paramount importance for calculating flow-derived biomarkers such as wall shear stress (WSS) which can affect the progression of vascular disease [1]–[6].

4D flow MRI spatiotemporal resolution and velocity encoding parameter (venc) are prescribed according to the vascular territory being imaged. Spatial and temporal resolutions are reported to range from 0.5–3.0mm^3 and 40–60ms, respectively [7], [8]. Jarvis *et al.* report setting the velocity encoding parameter (venc) as high as 150cm/s to capture the maximum expected velocity in the heart and aorta. [8]. Suboptimal spatiotemporal resolution of 4D flow MRI may result in reduced accuracy of the measured velocity field. The measured velocity error propagates into derived hemodynamic metrics. Szajer *et al.* compared the WSS obtained from 4D flow MRI and computational fluid dynamics (CFD) simulations. They found that 4D flow MRI-derived WSS was lower compared to CFD. This underestimation was attributed to the insufficient spatial resolution of 4D flow MRI and partial volume (PV) effects [9]. Van Ooij *et al.* reported that 4D flow MRI-derived WSS was underestimated by 50% compared to CFD-derived WSS. Increasing the imaging resolution resulted in higher WSS values [3]. Brindise *et al.* compared hemodynamic metrics derived from *in vivo* 4D flow MRI measurements in cerebral aneurysms to CFD and volumetric particle tracking velocimetry (PTV). Although the velocity fields were similar between modalities, considerable differences were found in the WSS-based metrics. The accuracy of WSS obtained from 4D flow MRI in smaller vessels was compromised due to insufficient spatial resolution [10].

Despite the imprecision imposed by 4D flow MRI's resolution and PV effects, no method exists to estimate the resulting bias error. This bias error arises due to intra-voxel phase dispersion (IVPD), which sums the signal of all isochromats (*i.e.*, spins precessing at the same frequency) [11] to yield a single value, thereby spatially under-resolving the flow measurement [12]. Several groups have introduced models to estimate or correct for IVPD. However, these approaches assume an ideal cylindrical geometry and only assess flow rate error across the vessel cross-section [11], [13], [14]. Methods to model the intra-voxel velocity distribution have been introduced by Dyverfeldt *et al.* but only quantify turbulent flow variables [15].

In this work, we develop a model to estimate the instantaneous and local bias error of 4D flow MRI velocity measurements by considering the intra-voxel velocity distribution and PV effects. This bias error is defined as the difference between the expectation of the velocity measurement and the actual velocity at the center of the voxel. The intra-voxel velocity distribution is assessed using a 3D Taylor Series expansion. PV effects and numerical error are modeled using a Richardson extrapolation according to the model's order of accuracy. Using 4D flow MRI noise estimates, we calculate a 68% confidence interval to assess the accuracy of the bias error estimation. The bias error model is validated using synthetic Womersley flow and applied to *in vitro* and *in vivo* 4D flow measurements in a cerebral aneurysm.

II. THEORY

We introduce a method to evaluate the bias error (β_i) for each component of the velocity vector ($i = x, y, z$) due to insufficient measurement resolution. This bias error estimation is resolved in space and time. We express β_i as its bias error estimate ($\hat{\beta}_i$) with 68% confidence interval bounds ($\sigma_{i,\beta}$):

$$\beta_i = \hat{\beta}_i \pm \sigma_{i,\beta} \tag{1}$$

Fig. 1 presents the workflow for evaluating the bias error estimate and 68% confidence interval for the MRI-measured velocity field. In Section II-A, we derive a bias error model for a single voxel by modeling the intra-voxel velocity distribution using a Taylor Series expansion. The bias error model is then generalized in Section II-B for all voxels in the field-of-view (FOV) and expressed as a system of linear equations. We account for numerical error and PV effects using a Richardson extrapolation in Section II-C according to estimates of the order of accuracy in PV voxels. The bias error is estimated for the measured velocity field. We model the propagation of measurement noise through the model to arrive at a 68% confidence interval for the bias error estimates. A 68% confidence interval corresponds to one standard deviation for normally distributed noise. Additional details of the derivations are provided in the Appendices.

A. Bias Error Model for a Single Voxel

We define the intra-voxel position vector ($\vec{a} \in \mathbb{R}^3$) relative to the center of the voxel as shown in Fig. 2a, with voxel dimensions in each Cartesian direction denoted by δ_x, δ_y, and δ_z. It is assumed that each component of the measured velocity ($v_{i,M}$) can be represented as the superposition of the actual velocity component (v_i), bias error (β_i), and the zero-mean random error component (ρ_i) at the voxel's center ($\vec{a} = \vec{0}$) [16]. The measured velocity component is expressed as:

$$v_{i,M} = v_i\left(\vec{a} = \vec{0}\right) + \beta_i + \rho_i \tag{2}$$

Herein, the correct velocity component at the voxel's center will be simply referred to as $v_{i,0}$ or the "voxel-centered" velocity component. Assuming the measured velocity is represented

by a stationary and ergodic process with zero-mean noise, the expectation of the measured velocity component ($\nu_{i,0} + \beta_i$) can be expressed as the integral of the intra-voxel velocity component distribution ($v_i(\vec{a})$) within the limits of the voxel, divided by the total voxel volume (V):

$$v_{i,0} + \beta_i = \frac{1}{V}\int_0^V v_i(\vec{a})dV \tag{3}$$

In (3), we assume that the bias error is dominated by IVPD effects as other error sources, such as concomitant gradients and eddy currents, are corrected prior to analysis [2]. The expected velocity was evaluated using (3) by Boussel *et al.* when downsampling high-resolution velocity fields to the resolution of 4D flow MRI [17]. Furthermore, in the 4D flow MRI consensus statement by Dyverfeld *et al.*, it is indicated that the expected velocity agrees well with the mean of the velocity field in voxels that are entirely composed of fluid flow [2]. This motivates the formulation of $\frac{1}{V}\int_0^V v_i(\vec{a})dV$ in (3), which is equivalent to the mean velocity in the voxel.

The intra-voxel velocity component is approximated using a 3D Taylor Series expansion centered about $\vec{a} = \vec{0}$ (*i.e.*, Maclaurin series):

$$v_i(\vec{a}) = v_{i,0} + \nabla v_i|_{\vec{a}=\vec{0}}\vec{a} + \frac{1}{2}\vec{a}^T\nabla\nabla v_i|_{\vec{a}=\vec{0}}\vec{a} + \cdots \tag{4}$$

The Taylor Series expansion represents the intra-voxel velocity distribution as a combination of $\nu_{i,0}$, odd gradient (*e.g.* ∇) and even gradient terms (*e.g.* $\nabla\nabla$). The bias error is calculated by substituting (4) into (3) and simplifying:

$$\beta_i = \frac{1}{V}\int_0^V \left(\nabla v_i|_{\vec{a}=\vec{0}}\vec{a} + \frac{1}{2}\vec{a}^T\nabla\nabla v_i|_{\vec{a}=\vec{0}}\vec{a} + \cdots\right)dV \tag{5}$$

It is worth noting that simplification eliminates $\nu_{i,0}$. Upon integrating, the odd gradient terms reduce to zero. Moreover, we found that the fourth-order and higher terms have negligible effects on the numerical approximation. As a result, even gradient terms greater than second-order are neglected. Thus, the bias error of a given voxel is:

$$\beta_i = \frac{1}{24}\left(\delta_x^2\frac{\partial^2}{\partial x^2} + \delta_y^2\frac{\partial^2}{\partial y^2} + \delta_z^2\frac{\partial^2}{\partial z^2}\right)v_i|_{\vec{a}=\vec{0}} + \mathcal{O}\left(\delta^4\right) \tag{6}$$

Equation (6) shows that each voxel dimension can be different when assessing the bias error. The fourth-order accuracy of (6) is indicated using $\mathcal{O}\left(\delta^4\right)$ [18]. We expect (6) to remain valid so long as the velocity gradient profile is monotonic.

Equation (6) is fourth-order accurate as the gradient terms fourth-order and higher are truncated in (5). Equation (6) matches Jasak *et al.*'s derivation of truncation error estimates for assessing the accuracy of Finite Volume solutions [19].

B. Bias Error Model for the Field-of-View

We expand the local bias error defined by (6) to describe the bias errors for all voxels in the FOV as a linear system. This expansion is possible considering the basis vectors expressing the intra-voxel, and FOV coordinates have the same orientation. We assign all the voxels in the FOV into one of three domains: the core flow (CF) domain, the partial volume (PV) domain, and the tissue domain (Fig. 2b). We assume the velocity distribution at all points in the tissue domain is zero. The domains are generated using a mask of the vessel geometry. Voxels outside of the mask are in the tissue domain, while voxels in the mask are either in the CF or PV domain. Any masked voxels that neighbor a tissue voxel are part of the PV domain. Masked voxels that neighbor only masked voxels are CF voxels.

From (6), the $v_i|_{\vec{a}=\vec{0}}$ term is expressed as a vector ($\boldsymbol{v}_{i,0}$) of length N for every voxel in the FOV. We use $\boldsymbol{v}_{i,0}$ to compute partial derivatives based on the voxel-centered velocities. The operator applied to $v_i|_{\vec{a}=\vec{0}}$ in (6) is written as an N-by-N matrix, $\boldsymbol{A}$, where each row numerically approximates partial derivatives using second-order accurate finite difference schemes. This allows us to express (6) as a linear system of equations and calculate the vectorized bias error component ($\boldsymbol{\beta}_i$) for all N voxels in the FOV:

$$\boldsymbol{\beta}_i + \boldsymbol{\varepsilon}_i = \boldsymbol{A}\boldsymbol{v}_{i,0} \tag{7}$$

where $\boldsymbol{\varepsilon}_i$ represents the numerical error of the finite difference schemes and added bias error due to PV effects, which (6) does not model. A similar approach was implemented by Zhang *et al.* for estimating pressure gradients from 4D flow MRI velocity measurements [20]. Finite difference schemes for CF voxels use velocities only from other CF voxels, while schemes for PV voxels use velocities from all domains. Rows of $\boldsymbol{A}$ which correspond to voxels in the tissue domain are set to zeros. This enforces the assumed uniform intra-voxel velocity of zero for tissue voxels.

We express the velocities measured with 4D flow MRI ($\boldsymbol{v}_{i,M}$) in the entire FOV using the same superposition principle that was used for a single voxel in (2):

$$\boldsymbol{v}_{i,M} = \boldsymbol{v}_{i,0} + \boldsymbol{\beta}_i + \boldsymbol{\rho}_i \tag{8}$$

where $\boldsymbol{v}_{i,M}$ and $\boldsymbol{\rho}_i$ are vectors of the same size as $\boldsymbol{\beta}_i$, $\boldsymbol{v}_{i,0}$, and $\boldsymbol{\varepsilon}_i$. Upon substituting (7) into (8) to eliminate $\boldsymbol{v}_{i,0}$, $\boldsymbol{\beta}_i$ is expressed as:

$$\boldsymbol{\beta}_i = (\boldsymbol{I}+\boldsymbol{A})^{-1}\boldsymbol{A}\boldsymbol{v}_{i,M} - (\boldsymbol{I}+\boldsymbol{A})^{-1}\boldsymbol{A}\boldsymbol{\rho}_i - (\boldsymbol{I}+\boldsymbol{A})^{-1}\boldsymbol{\varepsilon}_i \tag{9}$$

where $\boldsymbol{I}$ is an N-by-N identity matrix. Defining $(\boldsymbol{I}+\boldsymbol{A})^{-1}$ as $\boldsymbol{B}$, we rewrite (9) as:

$$\boldsymbol{\beta}_i = \boldsymbol{B}\boldsymbol{A}\boldsymbol{v}_{i,M} - \boldsymbol{B}\boldsymbol{A}\boldsymbol{\rho}_i - \boldsymbol{B}\boldsymbol{\varepsilon}_i \tag{10}$$

Equation (10) provides a linear equation for the bias error as a function of the one known parameter, $\boldsymbol{v}_{i,M}$, and two unknown parameters, $\boldsymbol{\rho}_i$ and $\boldsymbol{\varepsilon}_i$.

C. Bias Error Estimate and Confidence Interval

Numerical error is introduced into the bias error estimates as the partial derivatives in (6) are approximated using a finite difference scheme. There is also an added bias error due to PV effects contributing to the term $\boldsymbol{\varepsilon}_i$ in (10). Herein, we refer to $\boldsymbol{B\varepsilon}_i$ as the "numerical error term" in (10) and estimate it using a Richardson extrapolation. The Richardson extrapolation evaluates numerical error by comparing numerical solutions on grids with different spatial resolutions. To generate a coarse grid solution, we double the step size of the finite difference schemes in $\boldsymbol{A}$. We write $\boldsymbol{A}$ with twice the step size as $\boldsymbol{A}^{(2)}$, and the corresponding matrix $\boldsymbol{B}$ calculated using $\boldsymbol{A}^{(2)}$ as $\boldsymbol{B}^{(2)}$. Details of the derivation for the $\boldsymbol{B\varepsilon}_i$ estimate are provided in Appendix A.

As shown in the Appendix, $\boldsymbol{B\varepsilon}_i$ is expressed as:

$$\boldsymbol{B\epsilon}_i = \boldsymbol{P}\left(\boldsymbol{B}^{(2)}\boldsymbol{A}^{(2)} - \boldsymbol{BA}\right)\boldsymbol{v}_{i,M} - \boldsymbol{P}\left(\boldsymbol{B}^{(2)}\boldsymbol{A}^{(2)} - \boldsymbol{BA}\right)\boldsymbol{\rho}_i \tag{11}$$

in which $\boldsymbol{P}$ is a scaling factor dependent on the step size difference between $\boldsymbol{A}^{(2)}$ and $\boldsymbol{A}$, along with the order of accuracy of $\boldsymbol{A}$. Substituting (11) into (10), simplifying, and denoting $\boldsymbol{BA} - \boldsymbol{P}(\boldsymbol{B}^{(2)}\boldsymbol{A}^{(2)} - \boldsymbol{BA})$ as a matrix $\boldsymbol{C}$, the bias error is rewritten as:

$$\boldsymbol{\beta}_i = \boldsymbol{C}\boldsymbol{v}_{i,M} - \boldsymbol{C}\boldsymbol{\rho}_i \tag{12}$$

Henceforth, $\boldsymbol{C}\boldsymbol{v}_{i,M}$ will be referred to as the bias error estimate ($\hat{\boldsymbol{\beta}}_i$):

$$\hat{\boldsymbol{\beta}}_i = \boldsymbol{C}\boldsymbol{v}_{i,M} \tag{13}$$

Equation (13) corresponds to the bias error estimate defined in (1) for all voxels in the FOV.

The estimate provided by (13) is affected by the unknown random error ($\boldsymbol{\rho}_i$). We use the estimated statistical properties of $\boldsymbol{\rho}_i$ to define the 68% bias error confidence interval (CI) in (1). Each element in $\boldsymbol{\rho}_i$ is assumed to be normally distributed with a mean of zero and a variance of $\sigma^2_{i,\rho}$. The random error is assumed to be normally distributed for voxels with signal-to-noise ratio (SNR) greater than 5, according to Friman *et al.* [16]. The random error variance in the FOV is represented as a vector of length N ($\boldsymbol{\sigma}^2_{i,\rho}$). The value of $\sigma^2_{i,\rho}$ can be estimated using the SNR, according to Pelc *et al.* [21].

In Appendix B, the random error variance is propagated through the linear operator, $\boldsymbol{C}$, defined in (12). The 68% bias error CI vector ($\boldsymbol{\sigma}_{i,\beta}$) is then evaluated as:

$$\boldsymbol{\sigma}_{i,\beta} = sqrt\left(diag\left(\boldsymbol{C}\left[diag\left(\boldsymbol{\sigma}^2_{i,\rho}\right)\right]\boldsymbol{C}^T\right)\right) \tag{14}$$

in which $diag(\cdot)$ indicates the diagonal operator.

This 68% CI corresponds to one standard deviation assuming normally distributed noise. According to (13) and (14), the bias error in (1) is expressed as a bias error estimate with a 68% CI for all voxels.

III. METHODOLOGY

A. Synthetic Womersley Flow

The bias error model's performance was first assessed using synthetic Womersley flow, representing arterial flow in the cardiovascular system [22]. The velocity profile is dictated by the non-dimensional Womersley number ($\alpha = R\sqrt{\omega/\upsilon}$) indicating the ratio of pulsatile inertial forces to viscous forces, where R is the pipe radius, ω is the frequency owing to the flow pulsatility, and ν is the kinematic viscosity of the fluid. The flow in a cylindrical pipe has only the axial component along the z-axis, with no radial and circumferential components.

4D flow MRI provides phase images for each velocity component, along with a magnitude image, which quantifies the intensity of the MR signal. We synthetically generate this complex signal (Z) for each voxel as the summation of intra-voxel isochromatic complex signal (ζ_j) with additive complex noise (η) [23]. A total of N_{ISO} isochromats ($N_{ISO} = 20^3$) for each voxel were generated uniformly inside each voxel on a 20 × 20 × 20 grid with j indicating the isochromat index:

$$Z = \left(\sum_j^{N_{ISO}} \zeta_j\right) + \eta \tag{15}$$

The details on the generation of ζ_j and η are provided in Appendix C. PV effects are introduced when the voxel contains both tissue and flow isochromats. The extent of PV effects is quantified according to the saturation ratio (SR) defined for a PV voxel as the signal magnitude of the tissue adjacent to the vessel relative to the magnitude of the neighboring flow [24]. Different levels of PV effects are investigated by generating data with SR values ranging from 0 to 1. We generate ζ_j with a $venc$ of 100 cm/s. The variance of random error for each voxel was assessed using the SNR [21]:

$$\sigma_\rho^2 = \frac{2}{\pi^2}\frac{venc^2}{SNR^2} \tag{16}$$

The random error variance is used with (14) to generate bias error CIs in (1).

The isochromat velocity (u_j) is a function of the mean axial velocity in the pipe ($\bar{u}$), the radial distance of the j isochromat from the pipe centerline (r_j) and the pipe radius, R [25]:

$$u_j = Real\left\{\frac{\Lambda J_0(\Lambda) - \Lambda J_0(r_j/R)}{\Lambda J_0(\Lambda) - 2J_1(\Lambda)}\right\}\bar{u} \tag{17}$$

where $J_0(\cdot)$ and $J_1(\cdot)$, respectively, are the zeroth- and first-order Bessel functions of the first kind, $Real\{\cdot\}$ indicates the real component, and Λ is a complex number determined by the Womersley number:

$$\Lambda = \left(\frac{i-1}{\sqrt{2}}\right)\alpha \tag{18}$$

The mean velocity was set to 30 cm/s, which is in the range of blood flow velocity in carotid arteries. Equation (17) generates u_j for a single timeframe. Womersley numbers from 0 to 6 were considered, providing a range of physiologically relevant velocity profiles for cerebral circulation. Pipe diameters (D) ranged from 3 to 15mm, with isotropic voxel sizes ranging from 0.5 to 1mm.

4D flow MRI velocimetry includes a reference acquisition (Z_{ref}) to remove inhomogeneous magnetic field effects. The axial velocity measurements for the synthetic Womersley flow (v_M) is evaluated as the difference in phase between the flow-sensitive acquisition and reference acquisition, both multiplied by $\frac{venc}{\pi}$:

$$v_M = \frac{venc}{\pi}\left(\angle Z - \angle Z_{ref}\right) \tag{19}$$

We assume the reference acquisition is not sensitive to flow and model isochromats with zero phase in (15). The synthetic velocity measurements obtained from (19) are used to assess bias error estimates defined in (1).

We can compare our bias error estimates to a synthetic bias error (β_{synth}) as we know the intra-voxel velocity distribution and the size of the voxel. As a result, β_{synth} is independent of numerical error, noise, and PV effects, unlike the bias error estimates. The synthetic bias error is calculated for each voxel in the FOV as the difference between the expected velocity measurement and the velocity at the center of the voxel:

$$\beta_{synth} = E(v_M) - v_0 \tag{20}$$

The $E(v_M)$ is evaluated from $\sum_j^{N_{ISO}} \zeta_j$ in (15), and v_0 using (17).

The comparison to synthetic bias error is used to assess the accuracy of the bias error estimates. In CF voxels, we found that the numerical error is negligible. In PV voxels, the numerical error and PV effects are accounted for using a Richardson extrapolation, as explained in Section II-C. Appendix D outlines how the order of accuracy in the PV domain ($\hat{p}_{PV}$) is evaluated.

A total of 3,549 unique synthetic MR acquisitions were generated to investigate the effects of Womersley flow conditions and imaging parameters on $\hat{p}_{PV}$. These acquisitions were generated by varying the Womersley number between 0 and 6, relative pipe diameters $\left(D^* = {}^{D}/_{\delta_i}\right)$ in the range of 3.75 to 18.75, and the SR from 0 to 1.

The impact of voxel size and SR on the bias error in PV voxels was assessed by reporting the maximum synthetic bias error as a function of these parameters. We also demonstrate that the numerical error in CF voxels can be neglected relative to the synthetic bias error. The synthetic and estimated bias error were compared by plotting these as functions of the voxel's radial location in the pipe. The model's accuracy in PV voxels is quantified by assessing the maximum estimated bias error relative to the maximum synthetic bias error.

B. In Vitro 4D flow in ICA Aneurysm

The bias error model was applied to *in vitro* 4D flow measurements in 3D-printed flow phantoms replicating an internal carotid artery (ICA) aneurysm with complex flow patterns. According to IRB-approved protocol, *in vivo* 4D flow and time-of-flight (TOF) MRI data of the cerebral vasculature were acquired at Northwestern University. The flow phantom geometries were generated from TOF data segmented with open-source software ITK-SNAP [26]. Thresholding and region growth algorithms were used to segment the images. The images were imported into Geomagic Design software (3D Systems, Rock Hill, SC) to model the aneurysm's luminal surface with the proximal and distal ICA segments and add extensions connecting the model to a flow loop. A 1-to-1 and a scaled-up 2-to-1 *in vitro* phantoms were created. The phantoms were printed using a high-resolution ProJet MJP 2500 Plus printer (3D Systems, Rock Hill, SC) with VisiJet M2R-CL material.

A flow loop was created to conduct *in vitro* 4D flow measurements of the intra-aneurysmal flow at a steady flow rate. The flow rate for the 1-to-1 model was determined from the *in vivo* 4D flow data by calculating the flow rate in the proximal ICA at peak systole. The flow rate prescribed to the 2-to-1 model was determined by matching the Reynolds number to that of the 1-to-1 model to maintain flow similarity in both models. Both geometries had Reynolds numbers of 313, while the 1-to-1 and 2-to-1 geometries had flow rates of $4.45\frac{mL}{s}$ and $8.90\frac{mL}{s}$, respectively. The working fluid was a water-glycerol mixture (60:40 by volume) with a respective density and viscosity of $1110\frac{kg}{m^3}$ and 0.00372 $Pa \cdot s$. *In vitro* velocity measurements in both phantoms were acquired on Siemens 3T PRISMA scanner using dual-venc 4D flow MRI [27], with a flip angle of 15 degrees for these measurements. Table I contains a list of sequence parameters used to acquire the flow. Doubling the phantom size halves the velocities since the Reynolds number is held constant. The 1-to-1 and 2-to-1 phantoms were imaged with voxel sizes of $0.8 \times 0.8 \times 0.8\ mm^3$ and $0.85 \times 0.85 \times 0.8\ mm^3$, respectively. Similar voxel sizes achieve comparable SNR between the two phantoms while providing different spatial resolution levels of the flow. To maintain similar velocity-to-noise (VNR) values, we set the venc of the 2-to-1 phantom to be half that of the 1-to-1 phantom. The 4D flow MRI sequence used requires ECG-gating. We prescribed an artificial pulse to collect 18 timeframes (phases) of the steady flow in the *in vitro* phantoms according to the gating provided. However, only 15 timeframes exhibiting stationary noise were used since a stationary noise assumption was made in (3). These non-stationary effects are introduced during the k-t GRAPPA reconstruction.

The bias error model was applied to each velocity component in the 4D flow datasets acquired for the aneurysm flow. Values of $\hat{p}_{PV}$ from the synthetic study were used to define $\boldsymbol{P}$ in (11). The numerical error in CF voxels is neglected according to our findings presented in Section IV-A-2. The estimated bias error in the 1-to-1 and 2-to-1 phantoms were qualitatively compared for cross-sectional planes in the flow. Quantitative comparisons were made for the root mean square (RMS) values of the estimated bias error in the two phantoms.

C. In Vivo 4D flow in ICA Aneurysm

The bias error model was applied to *in vivo* 4D flow MRI measurements of the flow in the ICA aneurysm described above in Section III-B, as the *in vitro* experiments were conducted for the same patient. The 4D flow imaging parameters are shown in Table I. A pseudo-complex angiography algorithm generated a mask after thresholding combined velocity and magnitude data [28]. The bias error model was applied to all three velocity components at 16 timeframes within the cardiac cycle. This produced a spatiotemporally resolved bias error vector field for the *in vivo* 4D flow measurements. PV order of accuracy estimates from the synthetic study were used to define the scaling factor $\boldsymbol{P}$ in (11), and numerical error in CF voxels was expected to be negligible.

Quantitative comparisons between the bias error at systole and diastole were made to investigate its variability throughout the cardiac cycle. We also compared the magnitude of bias error in CF voxels to PV voxels and the magnitude of the bias error to the bias error CI.

IV. RESULTS

A. Synthetic Womersley Flow

1) Velocity and Signal Effects on Synthetic Bias Error—The synthetic Womersley velocity profiles and corresponding synthetic bias error profiles are shown in Fig. 3. The relative axial velocity (v^*) and relative synthetic bias error $\left(\beta^*_{synth}\right)$ were normalized by the mean velocity. The voxel center's relative radial location (r^*) was normalized by the pipe radius. Fig. 3a displays the velocity profiles for α of 0, 4, and 6. Fig. 3b shows the relative synthetic bias error corresponding to the velocity profiles in Fig. 3a for an isotropic voxel size of 0.75mm, pipe diameter of 1cm, and SR of 0.5. The synthetic bias error was evaluated using (20).

For $\alpha = 0$, the velocity profile is parabolic, which has a constant second-order derivative. This produces a constant bias error in CF voxels. At $\alpha = 4$ and 6, the velocity profile has variable second order derivatives in CF voxels and therefore fluctuating bias error. The bias error peaks in PV voxels located at the wall ($r^* = 1$). Fig. 3b includes values of r^* greater than 1 as the center of some PV voxels may reside outside the pipe but have edges of the voxel still in the flow.

Table II reports the maximum relative bias error at different levels of isotropic voxel sizes and SR for Womersley number $\alpha = 6$. At SR=0.5, there is a 91.3% increase in maximum bias error at $\delta_i = 1mm$ relative to $\delta_i = 0.5mm$. We observe that the maximum bias error increases with a decrease in SR. For a constant voxel size ($\delta_i = 0.75mm$), the maximum bias error increases by 125% at SR=0 relative to SR=1. These findings indicate that 4D flow MRI measurements' bias error is dictated by the intra-voxel velocity distribution and signal properties of flow relative to the tissue.

2) Order of Accuracy Estimates in PV Voxels—Fig. 4 presents the order of accuracy in PV voxels for the 3,549 synthetic MR datasets with different values of D^*, α, and SR. The lowest value for D^* was set to 3.75 because smaller values did not provide

enough CF voxels across the vessel diameter to inform bias error estimates in PV voxels adequately.

We found the values of $\hat{p}_{PV}$ to resemble a log-normal distribution, hence the natural log scale used in Fig. 4a and Fig. 4b. The median value of the $\hat{p}_{PV}$ distribution was 0.181. Hereafter, the bias error model estimates will evaluate $\hat{p}_{PV}$ for each PV voxel based on the best exponential fit of PV voxel's value of SR as presented in Fig. 4b:

$$\hat{p}_{PV} = 0.085\exp(1.39 * SR) \tag{21}$$

The SR dictates the degree of PV effects in the measurements (Table II). It can be observed that as SR increases from 0 to 1, the order of accuracy increases according to (21) as the PV effects are reduced. As the SR is increased from 0 to 1, the PV order of accuracy also increases from 0.085 to 0.34. While for an SR of 1 the PV effects are minimized, a high numerical error is still introduced due to steep changes of velocity gradients, which results in a low order of accuracy relative to that expressed in (6).

We evaluated the numerical error in CF voxels relative to the synthetic bias error. When considering all CF voxels across all 3,549 synthetic cases, we observed that the median absolute numerical error of the bias error estimate was only 2.45% of the median absolute synthetic bias error. This confirms our expectation that the numerical error in CF voxels is negligible.

3) Bias Error Model Validation

Fig. 5 compares the estimated and synthetic bias errors for the axial velocity at SNR_{CF} of 100, SR of 0.5, and pipe diameter of 1cm. The estimated and synthetic bias errors are represented according to their distance from the pipe center relative to the pipe radius. The synthetic and estimated bias errors are non-dimensionalized relative to the mean velocity. Bias error CIs are reported as bounds around the expected bias error estimate using (14).

Decreasing the voxel size reduces the estimated bias error. This bias error reduction is due to a smaller dynamic range of velocities in the voxel. The estimated bias error appears to agree with the synthetic bias error in CF voxels. For $\alpha = 0$, the estimated bias error in CF voxels for the 0.5mm voxel is reduced by 75.2% relative to the 1mm voxel. This reduction is similar to the 75% reduction observed in the synthetic bias error.

The bias error estimates capture the sharp increase in bias error in PV voxels relative to CF voxels for a range of Womersley numbers, voxel sizes, and SR. We quantify the accuracy of the bias error model in PV voxels according to the relative maximum bias error (β^*_{max}). The relative maximum bias error is quantified in PV voxels as the ratio of the maximum estimated bias error and the maximum synthetic bias error. In Fig. 6, a good agreement is observed for a voxel size of 0.75mm and 0.5mm. The bias error model underestimates the maximum PV bias error for 1mm voxels. There is no strong dependence of the model's accuracy on either SR or Womersley number. The variable accuracy of the model is due to residuals in approximating the best fit in Fig. 4b.

B. In Vitro 4D flow in Scaled ICA Aneurysm

For the steady flow measurements in the 1-to-1 and 2-to-1 phantoms of the ICA aneurysm, the measured velocities were arithmetically averaged over the timeframes to form spatially resolved velocity and bias error fields. To assess the model's order of accuracy using (21), SR is estimated for each PV voxel in the phantom measurements using the magnitude image. Noise in the magnitude image was minimized by first averaging magnitude images with respect to time, followed by applying a median filter to remove outliers. For each PV voxel, we considered a $3 \times 3 \times 3$ neighborhood centered on the PV voxel of interest. The PV voxel's SR is calculated as the neighborhood's minimum tissue magnitude and the maximum CF magnitude ratio. This value of SR is then used to evaluate $\hat{p}_{PV}$. Table III reports the 25%, 50%, and 75% quantiles of SR and $\hat{p}_{PV}$ for the 1-to-1 and 2-to-1 aneurysm flow phantoms. We see similar quantile values for the measurements in the two phantoms. The low SR values were expected as the phantoms were surrounded by air, which provides little signal.

Fig. 7 presents cross-sections of the relative velocity magnitude and relative bias error magnitude for the 4D flow acquisition within the 1-to-1 and 2-to-1 phantoms. The velocity magnitude and bias error magnitude fields were normalized by each flow phantom's mean inlet flow velocity. Since the Reynolds number was the same for both phantoms, the distributions of the velocity magnitude are similar.

Phantom scaling had a pronounced effect on the bias error. In CF voxels, the bias error for the 2-to-1 phantom was reduced due to the decreased range of intra-voxel velocities. The map of velocity magnitude for the 2-to-1 phantom shows a high-speed jet entering the aneurysm (x=30mm, y=25mm). The model captures elevated bias error in the flow layers surrounding the jet, which was characterized by steep changes of velocity gradients. Furthermore, there was a band of low bias error in the center of the jet corresponding to a more uniform velocity region. This behavior is best observed in the 2-to-1 geometry due to the higher resolution of the bias error field than that of the 1-to-1 geometry. Despite this, the velocity measurements in the 1-to-1 geometry still captured the elevated region of bias error at the bend of the ICA.

The RMS values for the CF and PV voxels in the 1-to-1 and 2-to-1 phantoms are listed in Table IV. The PV relative bias error is an order of magnitude higher than that in CF voxels. This is consistent with our synthetic results, which demonstrated a similar increase in PV voxels' bias error. The RMS bias error in the 2-to-1 phantom relative to the 1-to-1 phantom decreased by 46.4% in CF voxels but only 20.5% in PV voxels. Increased MR resolution restricts the dynamic range of velocities in voxels, thus reducing the bias error; however, this does not address the bias error due to PV effects, leading to lower error reduction in PV voxels.

We evaluated bias error CIs for each voxel and velocity component according to (14). The SNR in (16) was calculated using the "SNR Mult" method described by Dietrich *et al.*, using the 15 timeframes acquired for each geometry [29]. To account for averaging the velocity field for the 15 timeframes, we multiplied the SNR for each voxel by $\sqrt{15}$. Additionally,

since the magnitude image is the average across the four acquisitions obtained from the dual-venc sequence, we divided the SNR for each voxel by 2. The RMS SNR values in CF voxels were 115 and 94 for the 1-to-1 and 2-to-1 measurements. The RMS SNR values in PV voxels were 51 and 38 for the 1-to-1 and 2-to-1 measurements.

Bias error CIs were non-dimensionalized similar to the bias error using the mean inlet velocity. The RMS relative bias error CI for the CF and PV voxels ($\mathrm{RMS}\left(\sigma^*_{\beta,CF}\right)$ and $\mathrm{RMS}\left(\sigma^*_{\beta,PV}\right)$) in the 1-to-1 and 2-to-1 phantoms are presented in Table IV. Similar to the bias error, we observe an order of magnitude increase in the RMS CI in PV voxels compared to CF voxels. For the same domain type and phantom scale, the ratio between the RMS bias error and the RMS CI ratio ranged from 12.7 to 35.6. This indicates that the bias estimates are robust to measurement noise.

C. In Vivo 4D flow in ICA Aneurysm

The velocity magnitude and bias error magnitude fields were calculated for each voxel for the *in vivo* 4D flow MRI in the ICA aneurysm. These calculations were performed for each timeframe in the measured cardiac cycle. The median SR value at all time points was 0.279. The SNR was calculated as described in Section IV-B. However, the SNR at each voxel was not multiplied by $\sqrt{15}$ because the velocity fields were not averaged over the cardiac cycle. The RMS SNR was 6.36 and 6.13 in CF and PV voxels, respectively. We evaluated the bias error CI for each velocity component and voxel. The velocity magnitude, bias error magnitude, and bias error CI fields were normalized with respect to the mean inlet velocity across all timeframes. The velocity magnitude and bias error magnitude at peak systole and diastole are shown in Fig. 8.

Fig. 8 qualitatively shows that the bias error magnitude is higher at systole compared to diastole. Additionally, PV voxels appear to have a much higher bias error than CF voxels.

Table V reports the RMS bias error magnitude and RMS bias error CI for CF and PV voxels at systole and diastole. The RMS bias error magnitude in PV relative to CF voxels is 16.4 times larger at systole and 21.6 times larger at diastole. This increase in bias error in PV voxels is similar to that seen in our synthetic and *in vitro* studies. The bias error relative to the bias error CI is comparable in CF voxels, but the bias error in PV voxels is a factor of 2.90 to 5.08 times larger than the bias error CI at systole and diastole, respectively.

V. DISCUSSION AND CONCLUSION

In this study, we assess the local and instantaneous bias error of 4D flow MRI velocimetry due to IVPD. Our model demonstrates the bias error to be an interplay between the intra-voxel velocity distribution and PV effects. Specifically, the intra-voxel velocity distribution determines the bias error trend, and PV effects amplify this trend. The propagation of noise into the model is expressed using a 68% CI. The viability of the bias error model is demonstrated on synthetic velocity fields and those obtained from *in vitro* and *in vivo* 4D flow MRI measurements.

The intra-voxel velocity distribution effects on the bias error are expressed in (6) for a single voxel. Equation (6) shows that the bias error is a function of the velocity profile's concavity (*i.e.*, second-order derivative) and mediated by voxel size choice. This model serves as *a priori* guide to predict the bias error trend according to the velocity profile. We expect a positive bias error for velocity profiles that are concave upward and a negative bias error for velocity profiles that are concave downward; inflection points in the velocity profile correspond to zero bias error. This trend is observed in Fig. 3 for the Womersley number of 6, in which the velocity profile changing from an upward to downward concavity with increasing relative radial position corresponds to a transition from positive to negative bias error. Fig. 5 reports our bias error estimates alongside the synthetic bias error. Qualitatively, the estimates capture the trend of bias error in both CF and PV voxels. In CF voxels, the estimates closely follow the synthetic bias error at different Womersley numbers and capture the expected decrease in bias error with a reduction in voxel size, as predicted by (6).

In Section IV-B, scaling the *in vitro* phantom allowed us to reduce the range of the intra-voxel velocity distribution while maintaining similar voxel sizes and SR values between the two phantoms. This change in the intra-voxel velocity distribution reduces bias error magnitude for the larger size phantom, as observed qualitatively (Fig. 7) and quantitatively (Table IV). We expect the bias error to be highest in flow regions characterized by sharp changes in velocity gradients. This is most notably demonstrated in the 2-to-1 *in vitro* ICA aneurysm when comparing the velocity magnitude to the bias error magnitude map (Fig. 7). Steep changes of velocity at the edge of the jet entering the aneurysm correspond to elevated bias error magnitude. Contrastingly, in the core of this jet, we observe a relatively low bias error as the intra-voxel velocity profile is almost uniform.

Further evidence for the intra-voxel velocity distribution impact on the bias error is observed in the *in vivo* study (Section IV-C). Fig. 8 shows that the bias error is higher at systole than at diastole. Table V reports that the RMS bias error approximately doubles at systole compared to diastole in both CF and PV voxels. A higher flow rate increases the range of velocities in voxels, resulting in elevated bias error at systole compared to diastole, as suggested by our model. This dependence of the bias error on the phase of the cardiac cycle should be considered when evaluating hemodynamic metrics and planning 4D flow MRI scans.

Sharp changes in the intra-voxel velocity profile typically occur in PV voxels, where high-velocity gradients at the wall meet the stationary tissue. According to (6), this is expected to result in high levels of bias error. These near-wall voxels are also affected by PV effects, which exacerbate the bias error introduced by the intra-voxel velocity. This work quantified the PV effects using SR similar to Tang *et al.* [24]. The SR of each PV voxel is used to quantify the order of accuracy of the numerical scheme in (21) and assess the bias error using a Richardson extrapolation. The Richardson extrapolation acts to amplify the estimated bias error according to the PV voxel's SR. For synthetic Womersley flow, this amplification of the synthetic bias error is observed in Table II. With a decrease in SR (higher PV effects), the maximum bias error is increased for all voxel sizes. Figs. 5 and 6 demonstrate that our model is sensitive to the bias error in PV voxels for a range of SR values along with varying Womersley number and voxel size. The model predicts that the

bias error should generally be much higher in PV voxels than in CF voxels due to the sharp changes in velocity profile and PV effects. In the synthetic Womersley flow and *in vitro* and *in vivo* aneurysm studies, the bias error in PV voxels was an order of magnitude larger than that in CF voxels. This high bias error in PV voxels can contribute to errors in WSS derived from 4D flow MRI, as reported by other researchers [3], [9], [10].

Our model accounts for noise propagating into the bias error estimates by reporting a 68% bias error CI, as shown in (1). According to the model, higher levels of $\sigma_{i,\beta}$ are expected in PV voxels compared to CF voxels. This increase in CI bounds results from lower SNR values in PV voxels which, in turn, owes to higher noise variance according to (16). Additionally, the noise is amplified when propagated through the Richardson extrapolation used for PV voxels. Tables IV and V demonstrate that the CI bounds are wider in PV voxels than in CF voxels.

The bias error model presented in this work serves as an *a priori* guide for planning 4D flow MRI scans. The venc will affect the dynamic range and level of noise propagated into the measured velocity, and the choice of voxel size directly affects the bias error level, as shown in (6). Hoogeveen *et al.* show that SR is a function of proton density, relaxation parameters (T1 and T2), echo time (TE), repetition time (TR), and flip angle [30]. From these parameters, MR users can adjust TE, TR, and the flip angle to modulate SR and, as a result, the level of bias error in PV voxels.

The presented method is applicable for vessels with a diameter greater than or equal to 3.75 of the voxel size. Our synthetic Womersley flow study demonstrated that finite difference scheme stencils could not be generated for velocity fields with less than 3.75 voxels across the diameter. This constraint is likely to have broader applications to the estimation of metrics based on velocity gradients from 4D flow MRI data. Additionally, the bias error model assumes that the velocity gradient profile is monotonic, and the SNR is greater than 5. A further limitation of our model is its reliance on the order of accuracy estimates obtained from synthetic flow for *in vitro* and *in vivo* measurements. The best fit used to determine the model's order of accuracy in PV voxels has large residuals (Fig. 4b). These residuals cause underestimation of the maximum bias error for an isotropic voxel size of 1mm, as shown in Fig. 6.

Furthermore, despite investigating a range of SR values in the synthetic Womersley flow datasets, we assumed that the SR is constant throughout the FOV. Our model is limited by the definition of the tissue, CF, and PV domains (Fig. 2b) since this relies on an accurate mask of the vessel geometry. As described in Section II-B, the PV domain is evaluated directly from the mask of the entire vessel. If the vessel mask is inaccurate, then the assessment of the PV domain is likely also to be inaccurate. Fig. 5 shows that mischaracterization of these domains can lead to over- or under-estimation of the bias error in voxels near the vessel wall.

While Womersley flow represents pulsatile flow in straight vessels, it is not representative of all velocity profiles in the cardiovascular system. Our work is limited by only considering a subset of possible velocity profiles in the synthetic test cases. Furthermore, although our

in vitro test investigates more complex velocity fields, there is no ground truth solution. Although CFD simulations could provide high-resolution velocity fields, these simulations would not serve as a ground truth due to their own sources of error [10]. Rather, this work compares the change in bias error with model scale to the expected trend for similar signal properties and Reynolds number.

In conclusion, this study presents an approach to estimate the bias error of velocity measured with 4D flow MRI. The model indicates that bias error is introduced by the rate of change of velocity gradients. This bias error is mediated by the choice of the voxels size and amplified by PV effects in the near-wall voxels. The accuracy of the bias error estimates is reported according to its 68% confidence interval. The method is validated with synthetic Womersley flow and applied to *in vitro* and *in vivo* 4D flow in a cerebral aneurysm. The bias error model can assess the accuracy of 4D flow MRI measurements and serve as an *a priori* guide for planning 4D flow MRI scans. 4D flow MRI users could optimize their MR settings (*e.g.*, voxel size and signal-related settings) according to expected flow dynamics to mitigate the bias error level.

Acknowledgments

This work was supported by the National Institutes of Health awards R21 NS106696 and R01 HL115267.

APPENDIX A: RICHARDSON EXTRAPOLATION

Richardson extrapolations are used to estimate the exact solution in numerical methods [31]. For two numerical solutions, with an exact solution (f), solved on a fine grid (f_1) and coarse grid (f_2) the numerical error of the fine grid ($f_1 - f$) can be expressed as:

$$f_1 - f = \frac{1}{m^p - 1}(f_2 - f_1) \tag{A1}$$

where m is the refinement factor quantifying the coarse grid's size relative to the fine grid, and p is the order of accuracy of the numerical scheme used to solve for f_1 and f_2 [32].

When (10) is solved for $\boldsymbol{B}\boldsymbol{\varepsilon}_i$, with $\boldsymbol{\beta}_i$ being the exact solution, the numerical solution of the bias error on the native (fine) 4D flow MRI structured grid ($\boldsymbol{f}_1$) is:

$$\boldsymbol{f}_1 = \boldsymbol{B}\boldsymbol{A}\boldsymbol{v}_{i,M} - \boldsymbol{B}\boldsymbol{A}\boldsymbol{\rho}_i \tag{A2}$$

The coarse grid numerical solution of (10) is assessed by doubling the finite difference schemes' step size to generate the operator $\boldsymbol{A}$. We write $\boldsymbol{A}$ with twice the step size as $\boldsymbol{A}^{(2)}$ and the operator $\boldsymbol{B}$ calculated using $\boldsymbol{A}^{(2)}$ as $\boldsymbol{B}^{(2)}$. Therefore, the coarse numerical solution ($\boldsymbol{f}_2$) is expressed as:

$$\boldsymbol{f}_2 = \boldsymbol{B}^{(2)}\boldsymbol{A}^{(2)}\boldsymbol{v}_{i,M} - \boldsymbol{B}^{(2)}\boldsymbol{A}^{(2)}\boldsymbol{\rho}_i \tag{A3}$$

The numerical error term can be expressed as a scaling factor ($\boldsymbol{P}$) multiplied by the difference between $\boldsymbol{f}_2$ and $\boldsymbol{f}_1$, $\boldsymbol{P}(\boldsymbol{f}_2 - \boldsymbol{f}_1)$. $\boldsymbol{P}$ is defined as an N-by-N diagonal matrix with each

diagonal entry evaluating $1/m^p - 1$ for each voxel. Since the step size of $\boldsymbol{A}^{(2)}$ relative to $\boldsymbol{A}$ is doubled everywhere in the FOV, $m = 2$ for all voxels. The order of accuracy, p, is estimated by comparing $\boldsymbol{f}_1$ to the known bias error as described in Section III-A. Furthermore, in Section IV-A-2, we demonstrate that the additional bias error due to PV effects is modeled by the selection of p. Using the definitions of $\boldsymbol{f}_1$ and $\boldsymbol{f}_2$ in (A2) and (A3), we evaluate the numerical error term as:

$$\boldsymbol{B}\boldsymbol{\epsilon}_i = \boldsymbol{P}\left(\boldsymbol{B}^{(2)}\boldsymbol{A}^{(2)} - \boldsymbol{B}\boldsymbol{A}\right)\boldsymbol{v}_{i,M} - \boldsymbol{P}\left(\boldsymbol{B}^{(2)}\boldsymbol{A}^{(2)} - \boldsymbol{B}\boldsymbol{A}\right)\boldsymbol{\rho}_i \tag{A4}$$

APPENDIX B: BIAS ERROR CONFIDENCE INTERVAL

Given that $\boldsymbol{\beta}_i$ in (12) is independent of noise, the variance of $\hat{\boldsymbol{\beta}}_i$ is only due to $\boldsymbol{C}\boldsymbol{\rho}_i$ We define the variance of $\hat{\boldsymbol{\beta}}_i$ as $\boldsymbol{\sigma}^2_{i,\beta}$ and evaluate $\boldsymbol{\sigma}^2_{i,\beta}$ according to (12) and (13):

$$\boldsymbol{\sigma}^2_{i,\beta} = var(\boldsymbol{C}\boldsymbol{\rho}_i) \tag{A5}$$

For a linear system of equations (*e.g.*, $\boldsymbol{Y} = \boldsymbol{M}\boldsymbol{X}$), the variance-covariance of the output ($\boldsymbol{\Sigma}_Y$) is generally written as a function of the input variance-covariance matrix ($\boldsymbol{\Sigma}_X$) and the linear operator, $\boldsymbol{\Sigma}_Y = \boldsymbol{M}\boldsymbol{\Sigma}_X\boldsymbol{M}^T$ [33]. Given $\boldsymbol{C}$ is a linear operator and assuming no spatial correlation of noise, the variance of $\boldsymbol{C}\boldsymbol{\rho}_i$ is expressed as:

$$var(\boldsymbol{C}\boldsymbol{\rho}_i) = \boldsymbol{C}\left[diag\left(\boldsymbol{\sigma}^2_{i,\rho}\right)\right]\boldsymbol{C}^T \tag{A6}$$

where $diag(\cdot)$ in (A6) is the diagonal operator expressing $\boldsymbol{\sigma}^2_{i,\rho}$ as an N-by-N matrix. Equations (A5) and (A6) are combined by eliminating $var(\boldsymbol{C}\boldsymbol{\rho}_i)$ from both equations. The 68% bias error confidence interval vector ($\boldsymbol{\sigma}_{i,\beta}$) is evaluated as the square root of $\boldsymbol{\sigma}^2_{i,\beta}$:

$$\boldsymbol{\sigma}_{i,\beta} = sqrt\left(diag\left(\boldsymbol{C}\left[diag\left(\boldsymbol{\sigma}^2_{i,\rho}\right)\right]\boldsymbol{C}^T\right)\right) \tag{A7}$$

In (A7), $diag(\cdot)$ expresses the diagonal elements of $\boldsymbol{C}\left[diag\left(\boldsymbol{\sigma}^2_{i,\rho}\right)\right]\boldsymbol{C}^T$ as a vector of length N. The $sqrt(\cdot)$ operator evaluates each element's square root in $diag\left(\boldsymbol{C}\left[diag\left(\boldsymbol{\sigma}^2_{i,\rho}\right)\right]\boldsymbol{C}^T\right)$.

APPENDIX C: SYNTHETIC WOMERSLEY FLOW

Equation (15) assesses Z as the summation of isochromats in the voxel with additive noise. The isochromat complex signal (ζ_j) is assessed according to the isochromatic modulus ($|\zeta|_j$), velocity encoding parameter ($venc$), and intra-voxel axial velocity (u_j) at each j location:

$$\zeta_j = \left|\zeta\right|_j \exp\left(i\frac{\pi}{venc}u_j\right) \tag{A8}$$

The isochromat modulus is uniform in the flow and tissue regions. We evaluate $|\zeta|_j$ according to the prescribed values of saturation ratio (SR), CF voxel signal magnitude ($|Z|_{CF}$

= 100), and the number of isochromats modeled in each voxel ($N_{ISO} = 20^3$). In the flow domain, $|\zeta|_j$ is evaluated as the ratio of $|Z|_{CF}$ and N_{ISO}, and in the tissue domain, this ratio is multiplied by the SR:

$$|\zeta|_j = \begin{Bmatrix} |Z|_{CF}/N_{ISO},\ when\ j \in flow \\ (SR)(|Z|_{CF}/N_{ISO}), when\ j \in tissue \end{Bmatrix} \tag{A9}$$

We compute u_j according to the analytical Womersley solution in (17).

After summing ζ_j for all isochromats in the voxel, complex noise (η) is added to the signal. Both the real and imaginary components of η are normally distributed, zero-mean, uncorrelated, with a variance, σ_η^2 [34]. We quantify σ_η^2 using $|Z|_{CF}$ and the prescribed value of the SNR in CF voxels ($SNR_{CF} = 100$). For synthetic Womersley flow, both $|Z|_{CF}$ and SNR_{CF} were set to 100 to represent values found from *in vitro* MRI measurements [29]. The noise variance is then calculated using the ratio of CF magnitude and SNR_{CF} [35]:

$$\sigma_\eta^2 = \left(|Z|_{CF} \Big/ SNR_{CF}\right)^2 \tag{A10}$$

This value of σ_η^2 is constant for all voxels in the FOV. The SNR for each voxel is quantified as the ratio of the voxel's signal magnitude ($|Z|$) relative to σ_η.

APPENDIX D: ORDER OF ACCURACY ESTIMATES

The order of accuracy is evaluated by solving for p in (A1). We evaluate $\hat{p}_{PV}$ using an L2-norm [36]:

$$\hat{p}_{PV} = \frac{1}{\ln(m)} \ln\left(\frac{\|\boldsymbol{f}_2 - \boldsymbol{\beta}_{synth}\|_2}{\|\boldsymbol{f}_1 - \boldsymbol{\beta}_{synth}\|_2}\right) \tag{A11}$$

where $\boldsymbol{\beta}_{synth}$ is a vector of length N for the synthetic bias error at all voxels in the FOV and $\|\cdot\|_2$ evaluates the norm for vector elements only in the PV domain.

The order of accuracy estimates in (A11) are used to define rows corresponding to PV voxels of $\boldsymbol{P}$ in (A4). Rows of $\boldsymbol{P}$ corresponding to tissue and CF voxels are defined as zeros.

REFERENCES

[1]. Garcia J, Barker AJ, and Markl M, "The Role of Imaging of Flow Patterns by 4D Flow MRI in Aortic Stenosis," JACC: Cardiovascular Imaging, vol. 12, no. 2. Elsevier Inc., pp. 252–266, 01-Feb-2019. [PubMed: 30732721]

[2]. Dyverfeldt P, Bissell M, Barker AJ, Bolger AF, Carlhäll CJ, Ebbers T, Francios CJ, Frydrychowicz A, Geiger J, Giese D, Hope MD, Kilner PJ, Kozerke S, Myerson S, Neubauer S, Wieben O, and Markl M, "4D flow cardiovascular magnetic resonance consensus statement," Journal of Cardiovascular Magnetic Resonance, vol. 17, no. 1, Aug. 2015.

[3]. van Ooij P, Potters W. v., Guédon A, Schneiders JJ, Marquering HA, Majoie CB, Vanbavel E, and Nederveen AJ, "Wall shear stress estimated with phase contrast MRI in an in vitro and in vivo intracranial aneurysm," Journal of Magnetic Resonance Imaging, vol. 38, no. 4, pp. 876–884, 2013. [PubMed: 23417769]

[4]. Bieging ET, Frydrychowicz A, Wentland A, Landgraf BR, Johnson KM, Wieben O, and François CJ, “In vivo three-dimensional mr wall shear stress estimation in ascending aortic dilatation,” Journal of Magnetic Resonance Imaging, vol. 33, no. 3, pp. 589–597, Mar. 2011. [PubMed: 21563242]

[5]. Köhler B, Grothoff M, Gutberlet M, and Preim B, “Bloodline: A system for the guided analysis of cardiac 4D PC-MRI data,” Computers and Graphics (Pergamon), vol. 82, pp. 32–43, Aug. 2019.

[6]. Castle-Kirszbaum M, Maingard J, Lim R, Barras C, Kok HK, Chandra R, Chong W, and Asadi H, “Four-Dimensional Magnetic Resonance Imaging Assessment of Intracranial Aneurysms: A State-of-the-Art Review,” Neurosurgery, 2020.

[7]. Morgan AG, Thrippleton MJ, Wardlaw JM, and Marshall I, “4D flow MRI for non-invasive measurement of blood flow in the brain: A systematic review,” Journal of Cerebral Blood Flow and Metabolism. SAGE Publications Ltd, 01-Feb-2020.

[8]. Jarvis K, Soulat G, Elbaz M, and Markl M, “4D Flow MRI: Flow Dynamics,” Multimodality Imaging Innovations In Adult Congenital Heart Disease, pp. 133–153, 2021.

[9]. Szajer J and Ho-Shon K, “A comparison of 4D flow MRI-derived wall shear stress with computational fluid dynamics methods for intracranial aneurysms and carotid bifurcations — A review,” Magnetic Resonance Imaging, vol. 48. Elsevier Inc., pp. 62–69, 01-May-2018. [PubMed: 29223732]

[10]. Brindise MC, Rothenberger S, Dickerhoff B, Schnell S, Markl M, Saloner D, Rayz VL, and Vlachos PP, “Multi-modality cerebral aneurysm haemodynamic analysis: In vivo 4D flow MRI, in vitro volumetric particle velocimetry and in silico computational fluid dynamics,” Journal of the Royal Society Interface, vol. 16, no. 158, 2019.

[11]. Wolf RL, Ehman RL, Riederer SJ, and Rossman PJ, “Analysis of Systematic and Random Error in MR Volumetric Flow Measurements,” Magnetic Resonance in Medicine, 1993.

[12]. Stalder AF, Russe MF, Frydrychowicz A, Bock J, Hennig J, and Markl M, “Quantitative 2D and 3D Phase Contrast MRI : Optimized Analysis of Blood Flow and Vessel Wall Parameters,” vol. 1231, pp. 1218–1231, 2008.

[13]. Jiang J, Kokeny P, Ying W, Magnano C, Zivadinov R, and Mark Haacke E, “Quantifying errors in flow measurement using phase contrast magnetic resonance imaging: Comparison of several boundary detection methods,” Magnetic Resonance Imaging, vol. 33, no. 2, pp. 185–193, Feb. 2015. [PubMed: 25460329]

[14]. Polzin JA, Alley MT, Korosec FR, Grist TM, Wang Y, and Mistretta CA, “A Complex-Difference Phase-Contrast Technique for Measurement of Volume-Flow Rates,” Journal of Magnetic Resonance Imaging, 1995.

[15]. Dyverfeldt P, Gårdhagen R, Sigfridsson A, Karlsson M, and Ebbers T, “On MRI turbulence quantification,” Magnetic Resonance Imaging, vol. 27, no. 7, pp. 913–922, Sep. 2009. [PubMed: 19525079]

[16]. Friman O, Hennemuth A, Harloff A, Bock J, Markl M, and Peitgen H, “Probabilistic 4D blood flow tracking and uncertainty estimation,” Medical Image Analysis, vol. 15, no. 5, pp. 720–728, 2011. [PubMed: 21719342]

[17]. Boussel L, Rayz V, Martin A, Acevedo-Bolton G, Lawton MT, Higashida R, Smith WS, Young WL, and Saloner D, “Phase-contrast magnetic resonance imaging measurements in intracranial aneurysms in vivo of flow patterns, velocity fields, and wall shear stress: Comparison with computational fluid dynamics,” Magnetic Resonance in Medicine, vol. 61, no. 2, pp. 409–417, 2009. [PubMed: 19161132]

[18]. Chapra SC and Canale RP, Numerical Methods for Engineers. McGraw-Hill Higher Education, 2010.

[19]. Jasak H, “Error Analysis and Estimation for the Finite Volume Method with Applications to Fluid Flows,” 1996.

[20]. Zhang J, Brindise MC, Rothenberger S, Schnell S, Markl M, Saloner D, Rayz VL, and Vlachos PP, “4D-Flow MRI pressure estimation using velocity measurement-error based weighted least-squares,” arXiv. 2019.

[21]. Pelc N, Sommer F, Li K, Brosnan T, Herfkens R, and Enzmann D, “Quantitative magnetic resonance flow imaging.,” Magnetic Resonance Quarterly, vol. 10, pp. 125–147, 1994. [PubMed: 7811608]

[22]. Nichols WW, McDonald’s blood flow in arteries theoretical, experimental, and clinical principles, 6th ed. London: Hodder Arnold, 2011.

[23]. Müller-Bierl BM, Graf H, Pereira PL, and Schick F, “Numerical simulations of intra-voxel dephasing effects and signal voids in gradient echo MR imaging using different sub-grid sizes,” Magnetic Resonance Materials in Physics, Biology and Medicine, vol. 19, no. 2, pp. 88–95, May 2006.

[24]. Tang C, Blatter DD, and Parker DL, “Accuracy of phase-contrast flow measurements in the presence of partial-volume effects.,” Journal of Magnetic Resonance Imaging, vol. 3, no. 2, pp. 377–85, 1993. [PubMed: 8448400]

[25]. San O and Staples AE, “An improved model for reduced-order physiological fluid flows,” Journal of Mechanics in Medicine and Biology, vol. 12, no. 3, Jun. 2012.

[26]. Yushkevich PA, Piven J, Hazlett HC, Smith RG, Ho S, Gee JC, and Gerig G, “User-guided 3D active contour segmentation of anatomical structures: Significantly improved efficiency and reliability,” Neuroimage, vol. 31, no. 3, pp. 1116–1128, 2006. [PubMed: 16545965]

[27]. Schnell S, Ansari SA, Wu C, Garcia J, Murphy IG, Rahman OA, Rahsepar AA, Aristova M, Collins JD, Carr JC, and Markl M, “Accelerated dual-venc 4D flow MRI for neurovascular applications,” Journal of Magnetic Resonance Imaging, vol. 46, no. 1, pp. 102–114, 2017. [PubMed: 28152256]

[28]. Bock J, Kreher B, Hennig J, and Markl M, “Optimized pre-processing of time-resolved 2D and 3D phase contrast MRI data,” Proceedings of the 15th …, vol. 15, p. 3138, 2007.

[29]. Dietrich O, Raya JG, Reeder SB, Reiser MF, and Schoenberg SO, “Measurement of signal-to-noise ratios in MR images: Influence of multichannel coils, parallel imaging, and reconstruction filters,” Journal of Magnetic Resonance Imaging, vol. 26, no. 2, pp. 375–385, 2007. [PubMed: 17622966]

[30]. Hoogeveen RM, Bakker CJG, and Viergever MA, “MR Phase-Contrast Flow Measurement With Limited Spatial Resolution in Small Vessels: Value of Model-Based Image Analysis,” 1999.

[31]. Terziev M, Tezdogan T, and Incecik A, “A posteriori error and uncertainty estimation in computational ship hydrodynamics,” Ocean Engineering, vol. 208, Jul. 2020.

[32]. Phillips TS, Roy C, Tafti D, Mason W, and Cliff E, “Extrapolation-based Discretization Error and Uncertainty Estimation in Computational Fluid Dynamics,” 2012.

[33]. Johnson R and Wichern D, Applied Multivariate Statistical Analysis. Pearson Prentice Hall, 1998.

[34]. den Dekker AJ and Sijbers J, “Data distributions in magnetic resonance images: A review,” Physica Medica, vol. 30, no. 7, pp. 725–741, Nov. 2014. [PubMed: 25059432]

[35]. Lee AT, Bruce Pike G, and Pelc NJ, “Three-Point Phase-Contrast Velocity Measurements with Increased Velocity-to-Noise Ratio,” Magnetic Resonance in Medicine, vol. 33, no. 1, pp. 122–126, Jan. 1995. [PubMed: 7891526]

[36]. Ciarlet PG, The Finite Element Method for Elliptic Problems. 2002.

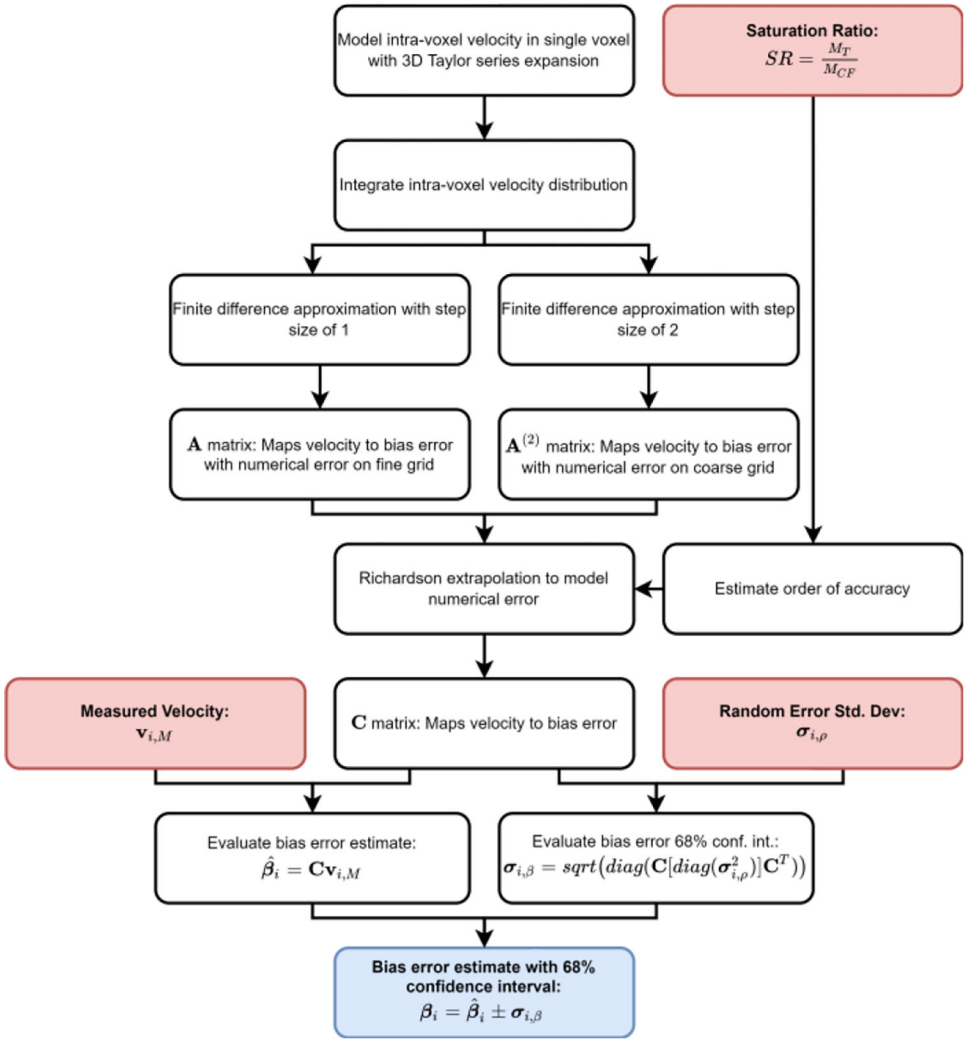

Fig. 1:

Bias error model workflow. Red boxes indicate inputs, black boxes indicate intermediate steps, and the blue box is the model output. The saturation ratio (SR) is defined for a PV voxel as the signal magnitude of the tissue (M_T) adjacent to the vessel relative to the magnitude of the neighboring core flow (M_{CF}).

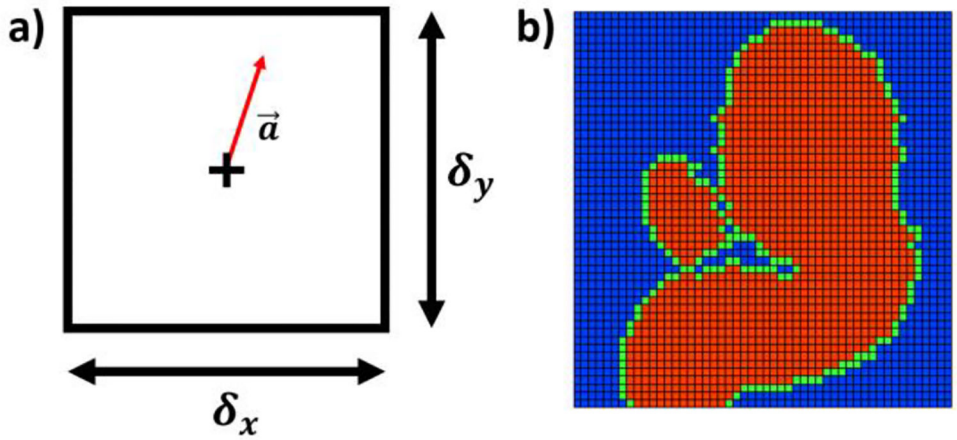

Fig. 2.

a) Intra-voxel coordinate system defined inside the voxel. The "+" denotes the voxel-center and the arrow indicates the intra-voxel position relative to the center; b) Cross-section of *in vitro* MR data for an internal carotid artery aneurysm indicating the tissue domain (blue), partial volume (PV) domain (green), and core flow (CF) domain (red).

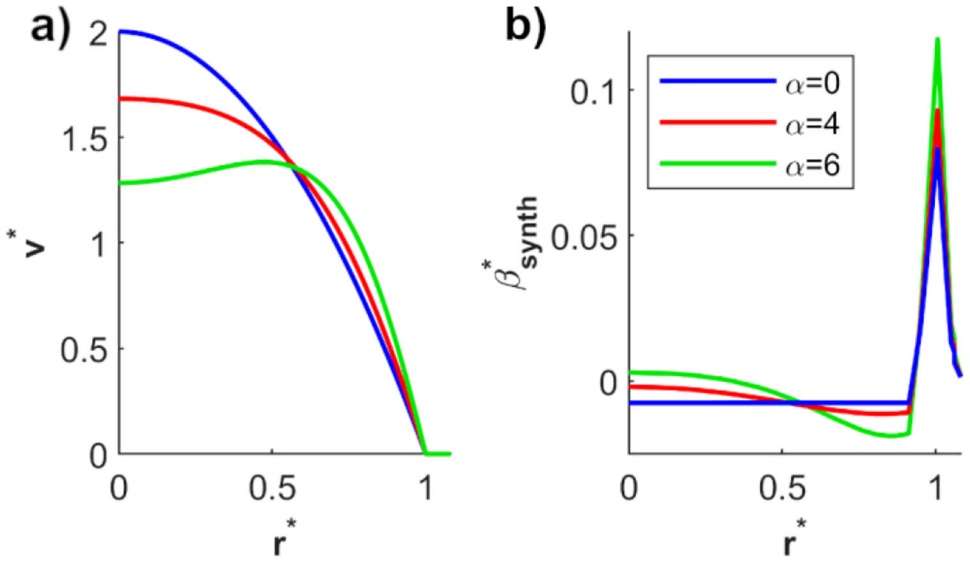

Fig. 3:

a) Relative velocity and b) corresponding relative synthetic bias error as a function of the relative radial location and Womersley number. The bias error was evaluated for an isotropic voxel size of 0.75mm, pipe diameter of 1cm, and SR of 0.5.

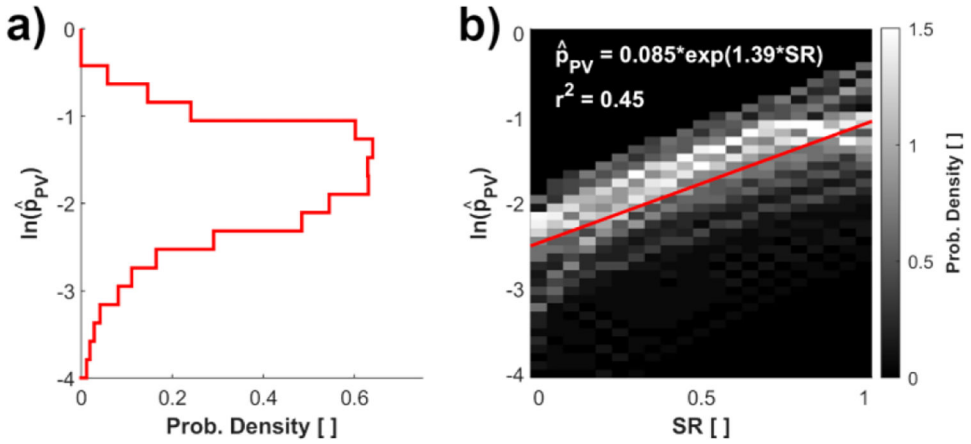

Fig. 4:

a) Probability density with respect to the natural log order of accuracy at PV voxels; b) Heat map of the PV natural log order of accuracy vs. SR. The intensity of the heat map indicates the probability density of the datapoint in the cell. Note that panel a is the projected probability density of panel b onto the y-axis.

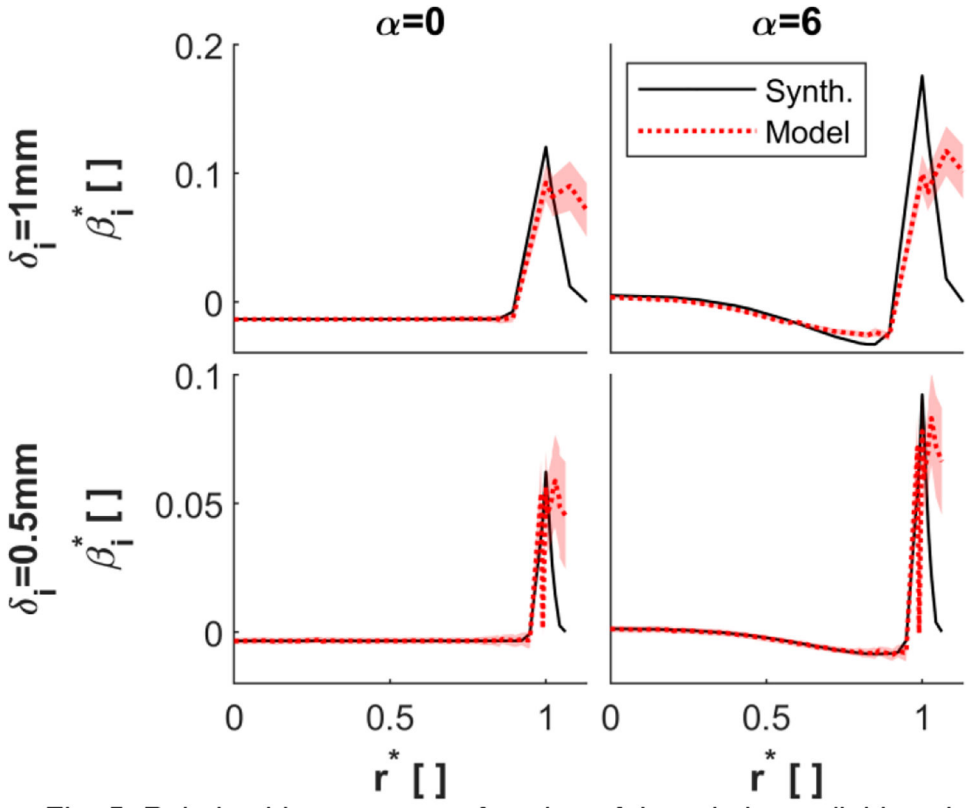

Fig. 5:

Relative bias error as a function of the relative radial location of the voxel-center for an SNR_{CF} of 100, pipe diameter of 1cm, and SR of 0.5. The bias error was evaluated using isotropic voxel sizes of 1mm (top row) and 0.5mm (bottom row) and Womersley numbers of 0 (left column) and 6 (right column). The solid lines indicate the synthetic bias error and the dotted lines indicate the expectation of the bias error estimate. The bounds indicate the 68% confidence interval. Note the change in y-axis limits for the two different voxel sizes.

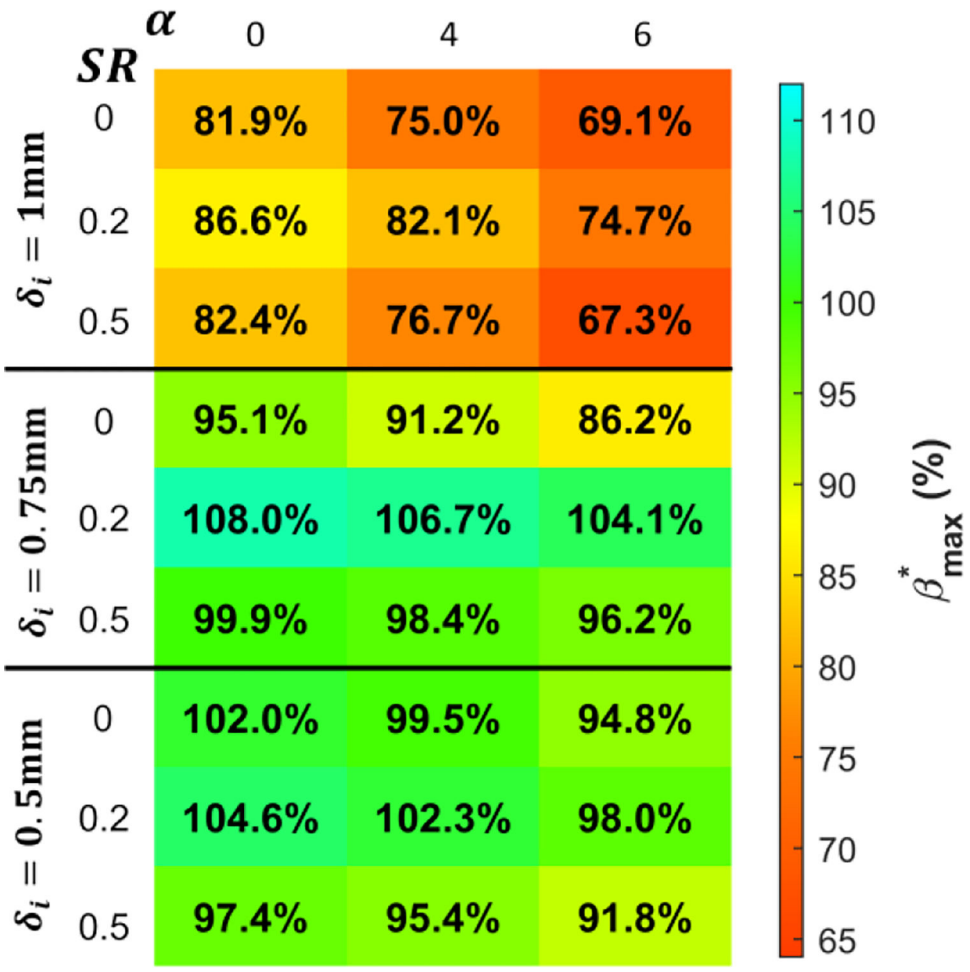

Fig. 6:

The relative maximum bias error is evaluated as a function of the Womersley number, SR, and voxel size.

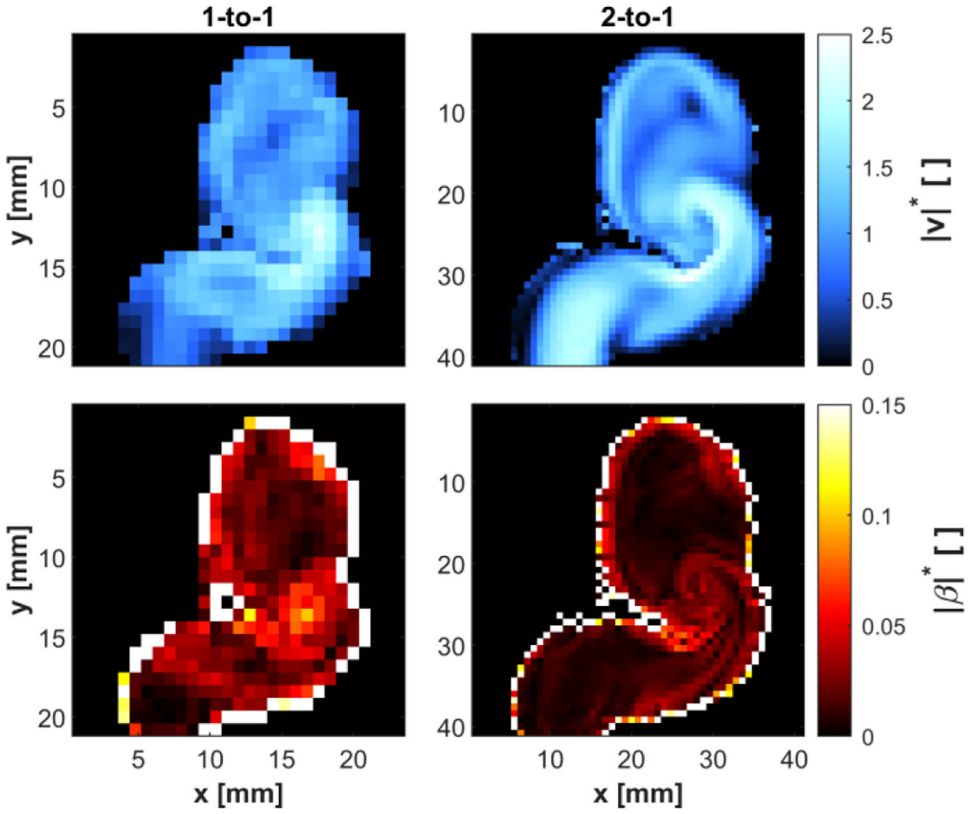

Fig. 7:

Cross-section of *in vitro* ICA aneurysm phantoms. The relative velocity magnitude was calculated from the 4D flow velocity in the 1-to-1 phantom (upper-left) and the 2-to-1 phantom (upper-right). The bias error magnitude was assessed from the 4D flow velocity in the 1-to-1 phantom (lower-left) and the 2-to-1 phantom (lower-right).

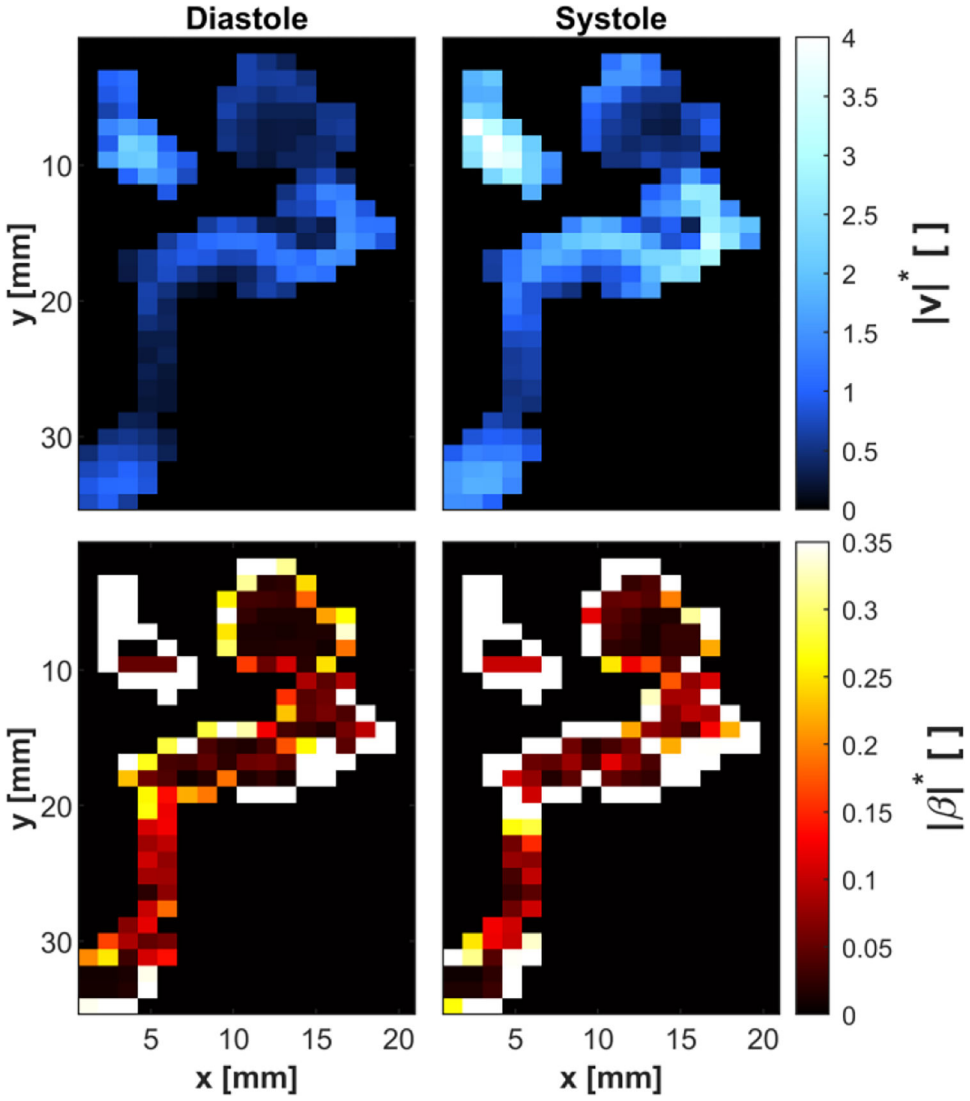

Fig. 8:

Cross-section of an *in vivo* ICA aneurysm. Note that although this is the same patient data as in Fig. 7, the chosen cross-sections differ slightly. The relative velocity magnitude was calculated from 4D flow MRI data at diastole (upper-left) and peak systole (upper-right). The bias error magnitude was assessed from the dual venc 4D flow velocity at diastole (lower-left) and peak systole (lower-right). The bias error is shown to be higher at systole relative to diastole, particularly at the jet entering the aneurysm.

TABLE I

Imaging parameters for *In vitro* and *in Vivo* Studies

	LOW VENC (*cm/s*)	HIGH VENC (*cm/s*)	TIME FRAMES	TE (*ms*)	TR (*ms*)
1-to-1 An.	30	60	18 (15)	4.08	6.8
2-to-1 An.	15	30	18 (15)	4.80	7.5
In vivo An.	50	100	16 (16)	3.39	6.1

Imaging parameters for the *in vitro* and *in vivo* aneurysm (An.) studies. The timeframe values in parenthesis indicate the number of cardiac phases used for analysis out of the total number of cardiac phases acquired per cardiac cycle.

TABLE II

Maximum Relative Bias Error as a Function of Voxel Size and SR ($\alpha = 6$)

	SR=1	SR=0.5	SR=0
$\delta_I = 0.5mm$	0.069	0.092	0.140
$\delta_I = 0.75mm$	0.085	0.117	0.191
$\delta_I = 1mm$	0.131	0.176	0.268

TABLE III

Saturation Ratio and Order of Accuracy Quantiles in 1-to-1 and 2-to-1 Aneurysm (An.) Phantoms

	$SR_{25\%}$	$SR_{50\%}$	$SR_{75\%}$	$\hat{p}_{PV,25\%}$	$\hat{p}_{PV,50\%}$	$\hat{p}_{PV,75\%}$
1-to-1 An.	0.085	0.099	0.119	0.096	0.098	0.100
2-to-1 An.	0.079	0.093	0.110	0.095	0.097	0.099

TABLE IV

RMS Relative bias Error Magnitude and RMS Relative bias Error Confidence intervals In 1-to-1 and 2-to-1 Aneurysm Phantoms

	$\mathrm{RMS}(\lvert\beta\rvert^*_{CF})$	$\mathrm{RMS}(\lvert\beta\rvert^*_{PV})$	$\mathrm{RMS}(\sigma^*_{\beta,CF})$	$\mathrm{RMS}(\sigma^*_{\beta,PV})$
1-to-1 An.	0.0424	0.438	0.00119	0.0202
2-to-1 An.	0.0227	0.348	0.00108	0.0274

TABLE V

RMS relative bias error magnitude and RMS relative bias error confidence intervals at diastole and systole for *in vivo* ICA 4D flow MRI measurements

	$\mathrm{RMS}(\lvert\beta\rvert^*_{CF})$	$\mathrm{RMS}(\lvert\beta\rvert^*_{PV})$	$\mathrm{RMS}(\sigma^*_{\beta,\,CF})$	$\mathrm{RMS}(\sigma^*_{\beta,\,PV})$
Systole	0.0732	1.20	0.0347	0.236
Diastole	0.0317	0.685	0.0347	0.236